Theoretical framework and experimental procedure for modelling mesoscopic volume fraction stochastic fluctuations in fiber reinforced composites

J. Guilleminot, Christian Soize, D. Kondo, C. Binetruy

Theoretical framework and experimental procedure for modelling volume fraction stochastic fluctuations in fiber reinforced composites

Johann Guilleminot [a], Christian Soize [b], Djimedo Kondo [c], Christophe Binetruy [a]

[a] *Ecole des Mines de Douai, Department of Polymers and Composites Technology & Mechanical Engineering, 941 rue Charles Bourseul, BP 10838, 59508 Douai Cedex, France*

[b] *Université Paris-Est, Laboratoire de Mecanique, 5 bd Descartes, 77454 Marne-la-Vallee, France*

[c] *Université des Sciences et Technologies de Lille, Laboratoire de Mécanique de Lille-UMR CNRS 8107, Cité Scientifique, Bd. Paul Langevin, 59655 Villeneuve d'Ascq Cedex, France*

Abstract

Many engineering materials exhibit fluctuations and uncertainties on their macroscopic mechanical properties. This basically results from random fluctuations observed at a lower scale, especially at the mesoscale where microstructural uncertainties generally occur. In the present paper, we first propose a complete theoretical stochastic framework (that is, a relevant probabilistic model as well as a non-intrusive stochastic solver) in which the volume fraction at the microscale is modelled as a random field whose statistical reduction is performed using a Karhunen-Loeve expansion. Then, an experimental procedure dedicated to the identification of the parameters involved in the probabilistic model is presented and relies on a non-destructive ultrasonic method. The combination of the experimental results with a micromechanical analysis provides realizations of the volume fraction random field. In particular, it is shown that the volume fraction can be modelled by a homogeneous random field whose spatial correlation lengths are determined and may provide conditions on the size of the meso-volumes to be considered.

Key words: composite materials, experimental identification, Karhunen-Loeve expansion, micromechanics, Polynomial Chaos expansion, probabilistic model, stochastic modelling, volume fraction
PACS:

1 Introduction

The introduction of randomness into a mechanical modeling process has received a quite large attention from the scientific community. In particular, Stochastic Mechanics has become more widespread mainly due to the development of the Stochastic Finite Elements Method (SFEM) - see, for a general overview, the book from Ghanem and Spanos [1], as well as the general reviews [2] [3]. These methods however deal with random properties which fluctuate at a macroscopic scale (that is for instance, a Young's modulus over a composite plate) and thus, one can wonder on how such random macroscopic properties can be assessed without completely resorting to expensive and time-consuming material qualification loops. In order to achieve such a rather difficult task, multi-scale approaches seem to be promising, provided they can properly integrate, in a way to be defined, the random dimension of the physical phenomenom [23]. Surprisingly, only a few papers were basically dedicated to such a multi-scale probabilistic approach and the topic (in particular, the construction of relevant probabilistic models) still remains quite unexplored [4] [5] [6].
Dealing with composite materials, it is well-known that the randomness is mainly due to the manufacturing process (combined to the batch-to-batch variability). The nature of the uncertainties itself basically depends on the technology or equivalently, on the nature of the composite. Laminates are typically manufactured using a consolidation process (inside an autoclave for instance), yielding in most cases to uncertainties on the definition of the composite part itself (geometry, thicknesses, etc.). In the case of injection moulding, one may consider three main microstructural features: the final length of the fibers, their orientation and their distribution inside the material. Here, one typically distinguishes two main cases [22]:

- case of short fiber composites: the initial length of the fibers is quite well preserved, the orientation is well predicted considering the flow lines, the distribution of the fibers is homogeneous over the composite part;
- case of long fiber composites: due to fiber breakage during the process (shearing action in the screw), a length distribution is often observed. Also, defining an orientation tensor may be meaningless because the fibers are curved and so, no particular randomness on orientation can be clearly introduced (in most cases, the composite may be approximated as isotropic). Finally, fiber clustering can be observed, leading to random fluctuations of the volume fraction (see Fig. (1)).

In this paper, we investigate the case of long fiber thermoplastic materials, for which uncertainties on the volume fraction at a meso-scale are clearly observed

Email address: guilleminot@ensm-douai.fr (Johann Guilleminot).

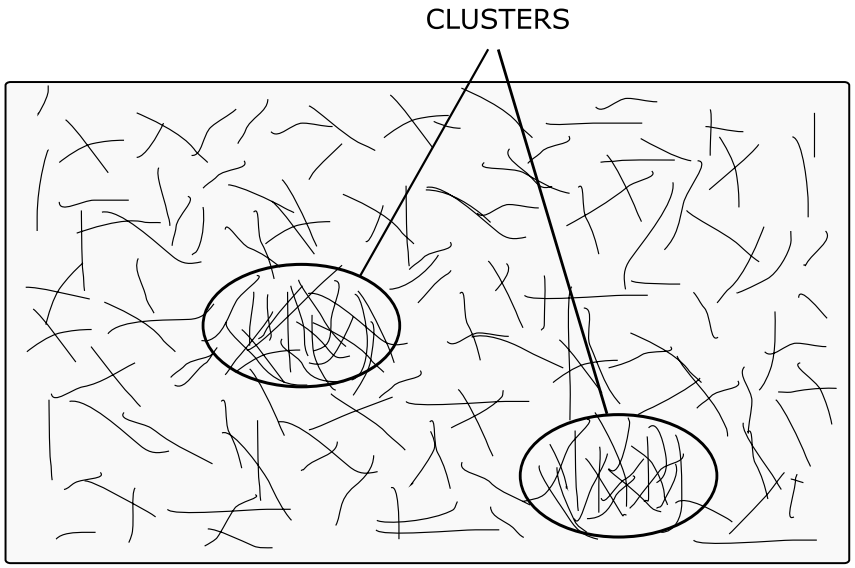

Figure 1. Fiber clustering in long fiber suspensions (redrawn from [21] [22]).

along both the injection flow and thickness directions [7]. It is assumed that a fiber length distribution exists but has a negligible effect on the random macroscopic mechanical behaviour. The main objective of the paper is then to propose a new methodology that allows to evaluate the impact of such a microstructural uncertainty at the meso-scale of composite materials.

2 Scales setting

In order to take into account these local fluctuations, as well as to properly catch the randomness at the meso-scale, we consider three different scales (namely the microscale, the meso-scale and the macroscale), that are assumed to be well separated and such as described in Gărăjeu and Suquet [8]. Considering such a double-scale homogenization, one introduces a partition of Ω, $\Omega = \cup_{j=1}^{N^*} \Omega_j$ (where Ω_j is called "sub-" or "meso-volume"), as shown on Fig. (2). This scale separation allows to proceed to two successive homogenization steps:

- the first one is performed between the microscale and the meso-scale and allows to estimate the mechanical effective properties of each meso-volume;
- the second one is performed between the meso-scale and the macroscale and thus, it integrates the random meso-structure of the composite.

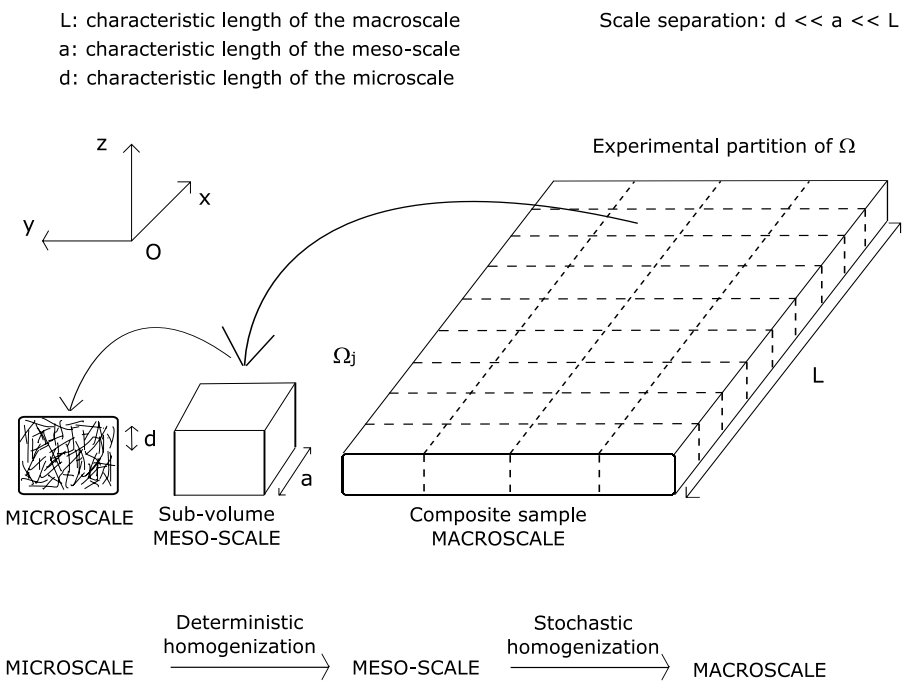

Figure 2. Top: experimental partition and scale separation. Bottom: successive homogenization procedures.

Considering a two-phase composite material, the volume fractions of reinforcement at the micro- and meso-scale will be denoted by f and F respectively. Section (3) presents the general mathematical framework as well as the stochastic multiscale modelling. The experimental analysis (used for the identification of parameters involved in the probabilistic model) is then detailed and discussed in section (4).

3 Proposed stochastic modelling and mathematical framework

Since the volume fraction at the meso-scale fluctuates along both the spatial axis and the probabilistic dimension, it has to be modelled as a random field. In general, a probabilistic modelling procedure relies on three critical steps:

(1) establishing a suitable representation for the random quantity, as detailed in section (3.1);
(2) defining a strategy in order to identify the parameters involved in the representation (see section 3.2);
(3) choosing the most relevant stochastic solver taking into account the probabilistic dimension of the problem, as discussed in section 3.3.

3.1 Construction of a probabilistic model

Since the size of the meso-volume is unknown *a priori*, it is proposed to model the microscopic random field f, the corresponding random field at the meso-scale F being determined in turn using an average rule (see (3.1.2)).

3.1.1 Definition of a class of random fields for modelling the microscopic random field

Let $f(\mathbf{x})$, $\mathbf{x} \in \Omega$ be a random field defined on a probability space $(\Theta, \mathcal{F}, \mathcal{P})$, indexed by a bounded set Ω in $\mathbb{R}^2$ with values in $[0,1] \subset \mathbb{R}$. For $\theta_k \in \Theta$, the mapping $\mathbf{x} \mapsto f(\mathbf{x}, \theta_k)$ from Ω into $[0,1]$ defines a trajectory of the random field. It is assumed that f is a second-order random field. Let $\mathbf{x} \mapsto \underline{f}(\mathbf{x}) = E\{f(\mathbf{x})\}$ be its mean function from Ω into $[0,1]$, in which E denotes the mathematical expectation. Let $(\mathbf{x}, \mathbf{x'}) \mapsto R_f(\mathbf{x}, \mathbf{x'}) = E\{f(\mathbf{x}) f(\mathbf{x'})\}$ be its autocorrelation function from $\Omega \times \Omega$ into $\mathbb{R}$. Finally, let $(\mathbf{x}, \mathbf{x'}) \mapsto C_f(\mathbf{x}, \mathbf{x'}) = E\left\{\left(f(\mathbf{x}) - \underline{f}(\mathbf{x})\right)\left(f(\mathbf{x'}) - \underline{f}(\mathbf{x'})\right)\right\} = R_f(\mathbf{x}, \mathbf{x'}) - \underline{f}(\mathbf{x})\,\underline{f}(\mathbf{x'})$ be its covariance function from $\Omega \times \Omega$ into $\mathbb{R}$. It is assumed that the correlation function satisfies the following condition:

$$\int_\Omega \int_\Omega |R_f(\mathbf{x}, \mathbf{x'})|^2 \, d\mathbf{x} d\mathbf{x'} < +\infty \tag{1}$$

which makes the correlation operator a Hilbert-Schmidt operator, allowing one to proceed to a statistical reduction of the random field, as further detailed in section (3.1.4).

3.1.2 Definition of the set of experimental realizations

We consider $p^{\exp}$ composite plates which are interpreted as $p^{\exp}$ independent realizations of the microscopic random field. Since the volume fraction is an additive property, realizations of the mesoscopic random field F are determined from the following average rule:

$$\forall k \in \{1, ..., p^{\exp}\}, \ \forall j \in \{1, ..., N^*\}, \ F^{\exp(j)}(\theta_k) = \frac{1}{t_m} \sum_{t=1}^{t_m} f^{\exp(t)}(\theta_k) \tag{2}$$

where t_m is a parameter and a partition on the meso-volume Ω_j (involving a set of micro-volumes $\{\omega_l\}_l$), $\Omega_j = \bigcup_l \omega_l$, was introduced and is such that $f^{\exp(t)}(\theta_k) = f(\mathbf{x}, \theta_k)$, $\mathbf{x} \in \omega_t$. Recalling the partition introduced in section (2), the set of experimental results is then defined as:

$$\mathcal{S}^{\exp} = \{f^{\exp}(\mathbf{x}_i, \theta_j), \ i \in \{1, ..., N\}, \ j \in \{1, ..., p^{\exp}\}\} \tag{3}$$

3.1.3 *Estimation of the mean and correlation functions from experimental results*

Unbiased estimates of the mean and correlation functions are determined from $\mathcal{S}^{\text{exp}}$ and are respectively given by:

$$\widehat{\underline{f}}_{p^{\text{exp}}}(\mathbf{x}_i) = \frac{1}{p^{\text{exp}}} \sum_{k=1}^{p^{\text{exp}}} f(\mathbf{x}_i, \theta_k) \tag{4}$$

$$\widehat{C}_f(\mathbf{x}_i, \mathbf{x}_j) = \frac{1}{1-p^{\text{exp}}} \sum_{k=1}^{p^{\text{exp}}} \left(f(\mathbf{x}_i, \theta_k) - \widehat{\underline{f}}_{p^{\text{exp}}}(\mathbf{x}_i) \right) \left(f(\mathbf{x}_j, \theta_k) - \widehat{\underline{f}}_{p^{\text{exp}}}(\mathbf{x}_j) \right) \tag{5}$$

for $(i,j) \in \{1, ..., N\}^2$.

3.1.4 *Statistical reduction of the random field*

Since the number of parts N involved in the partition may become quite large, it is convenient to proceed to a reduction of the random field by means of a Karhunen-Loeve expansion [10]. Thus, the random field is next written as:

$$f_M(\mathbf{x}) \approx \underline{f}(\mathbf{x}) + \sum_{\alpha=1}^{M} \sqrt{\lambda_\alpha} \eta_\alpha \psi_\alpha(\mathbf{x}) \tag{6}$$

where M should be lower than N. Let $\{\lambda_\alpha\}_{\alpha=1}^{M}$ and $\{\psi_\alpha\}_{\alpha=1}^{M}$ be the eigenvalues and eigenvectors of the covariance operator, that is, they satisfy the following eigenvalue problem (see [10]):

$$\int_\Omega C_f(\mathbf{x}, \mathbf{x'}) \psi_\alpha(\mathbf{x'}) \, d\mathbf{x'} = \lambda_\alpha \psi_\alpha(\mathbf{x}) \tag{7}$$

which has to be solved numerically in the present case [1]. Making use of a collocation method, Eq. (7) is classically converted into the following matrix eigenproblem:

$$\widehat{C}_f \, \Psi = \Lambda \Psi \tag{8}$$

where Ψ and Λ are the modal matrix (whose colums will be denoted by $\vec{\psi_\alpha}$) and the canonical form of $\widehat{C}_f$ respectively. It is worth noticing that Eq. (6) basically corresponds to a truncated representation introducing an error of approximation. It can then be proved that the norm of the error takes the form [11]:

$$E\left\{ ||f - f_M||_H^2 \right\} = \int_\Omega tr\left[C_f(\mathbf{x}, \mathbf{x}) \right] d\mathbf{x} - \sum_{k=1}^{M} \lambda_k \tag{9}$$

Eq. (9) allows one to estimate the norm of the error resulting from the truncation and thus, the determination of an optimal order of expansion M. Note that such a value can also be obtained analysing the convergence of the function $p \longmapsto \sum_{i=1}^{p} \lambda_i^2$.

The random vector $\eta = (\eta_1, ..., \eta_M)$ is such that:

$$E\{\eta_\alpha\} = 0,\ E\{\eta_\alpha \eta_\beta\} = \delta_{\alpha\beta} \tag{10}$$

(where δ is the Kronecker delta) and has a probability distribution which depends on the probability law of the random field f and which can be constructed as explained in [11]. Making use of the orthogonality of the basis $\{\psi_\alpha\}_{\alpha=1}^M$ in Eq. (6), one computes the independent realizations $\eta_\alpha(\theta_j)$:

$$\eta_\alpha(\theta_j) = \frac{1}{\sqrt{\lambda_\alpha}} \left\langle \mathbf{f}(\theta_j) - \underline{\widehat{\mathbf{f}}}, \vec{\psi_\alpha} \right\rangle \tag{11}$$

where $\mathbf{f}(\theta_j) = (f(\mathbf{x}_1, \theta_j), ..., f(\mathbf{x}_N, \theta_j))$, $\underline{\widehat{\mathbf{f}}} = \left(\underline{\widehat{f}}(\mathbf{x}_1), ..., \underline{\widehat{f}}(\mathbf{x}_N)\right)$ and $\langle \cdot, \cdot \rangle$ denotes the classical inner product in $\mathbb{R}^N$. The centred random vector η can be classically represented using a Polynomial Gaussian Chaos expansion ([11] [12]) which is written at the q-th order as:

$$\eta = \sum_{\gamma, |\gamma|=1}^{q} \mathbf{z}_\gamma \frac{H_\gamma(\mathbf{X})}{\sqrt{\gamma!}} \tag{12}$$

where γ is a multi-index $(\gamma_1, ..., \gamma_m) \in \mathbb{N}^m$ (with $|\gamma| = \sum_{k=1}^m \gamma_k \leq q$ and $\gamma! = \prod_{k=1}^m \gamma_k!$), $\mathbf{X}$ is a m-dimensional zero-mean Gaussian vector ($E\{X_i X_j\} = \delta_{ij}$), $H_\gamma(\mathbf{X}) = \prod_{k=1}^m h_{\gamma_k}(X_k)$ (where $h_{\gamma_k}(x)$ is the one-dimensional Hermite polynomial of order γ_k) and $\mathbf{z}_\gamma$ is a vector in $\mathbb{R}^M$. Combining the relation $E\{\eta_\alpha \eta_\beta\} = \delta_{\alpha\beta}$ with Eq. (12) yields:

$$\sum_{\gamma, |\gamma|=1}^{q} \mathbf{z}_\gamma {\mathbf{z}_\gamma}^T = I_M \tag{13}$$

where I_M is the $M \times M$ unit matrix. Denoting by Q the number of terms in the sum above, it is readily seen that a necessary condition for Eq. (13) to hold is that:

$$M \leq Q = \frac{(m+q)!}{m!q!} - 1 \tag{14}$$

which provides an usefull inequality between the size m of the Gaussian germ $\mathbf{X}$, the order q of the Polynomial Chaos expansion and the order of truncature M of the Karhunen-Loeve representation. Since it is known that adding terms in the Polynomial Chaos expansion does not necessarily improve the approximation (in practice, a convergence analysis has to be performed) [16] and since an optimal value for M can be derived from Eq. (9), Eq. (14) can then be used for choosing a suitable size m of the germ.

Remark: despite the fact that there is a straightforward formal analogy between Eq. (6) and the formulation used by Gărăjeu and Suquet [8] (see their Eq. (3.1)), it must be emphasized that Eq. (6) integrates explicitly the randomness of the fluctuations.

3.2 Identification of the Chaos coefficients

Let $\left\{\Xi^1, \Xi^2, ..., \Xi^{p^{\exp}}\right\}$ be $p^{\exp}$ experimental realizations of random vector η (with $\Xi^i = \eta\left(\theta_i\right)$ and $\Xi^i_j = \eta_j\left(\theta_i\right)$), computed from $\mathcal{S}^{\exp}$ using Eq. (11). Let $\mathbf{Z}$ be the $M \times Q$ matrix whose colums are the vectors $\mathbf{z}_\gamma$. Eq. (13) can be rewritten as:

$$\mathbf{Z}\mathbf{Z}^{\mathrm{T}} = I_M \tag{15}$$

Let p_η be the probability density function of η. Finally, let $\mathcal{C}$ be the manifold defined by Eq. (13). The estimation of $\mathbf{Z}$ can be performed using the Maximum Likelihood method, as detailed in [9]. The identification problem can then be stated as follows:

$$\mathcal{R}_1 : \max_{\mathbf{Z}\in\mathcal{C}} \mathcal{L}\left(\Xi^1, ..., \Xi^{p^{\exp}}; \mathbf{Z}\right) \tag{16}$$

where $\mathcal{L}$ is the likelihood function defined as:

$$\mathcal{L}\left(\Xi^1, ..., \Xi^{p^{\exp}}; \mathbf{Z}\right) = \prod_{i=1}^{p^{\exp}} p_\eta\left(\Xi^i, \mathbf{Z}\right) \tag{17}$$

In practice, such an optimization problem is very time-consuming because of the estimation of the joint probability density functions. Thus, one substitutes $\mathcal{L}$ by $\widetilde{\mathcal{L}}$, given by [9]:

$$\widetilde{\mathcal{L}}\left(\Xi^1, ..., \Xi^{p^{\exp}}; \mathbf{Z}\right) = \prod_{i=1}^{p^{\exp}} \prod_{j=1}^{M} p_{\eta_j}\left(\Xi^i_j, \mathbf{Z}\right) \tag{18}$$

Note that the approximation defined by Eq.(18) is relatively efficient because the random variables η_α, while statistically dependent, are uncorrelated. This yields the following approximation $\mathcal{R}_2$ of $\mathcal{R}_1$:

$$\mathcal{R}_2 : \max_{\mathbf{Z}\in\mathcal{C}} \widetilde{\mathcal{L}}\left(\Xi^1, ..., \Xi^{p^{\exp}}; \mathbf{Z}\right) \tag{19}$$

Furthermore, for computational purposes, one classically considers the log-likelihood function $\widetilde{\mathcal{L}}_{\log} = \log_{10}\left(\widetilde{\mathcal{L}}\right)$, resulting in the final approximation $\mathcal{R}_3$ of the initial optimization problem $\mathcal{R}_1$:

$$\mathcal{R}_3 : \max_{\mathbf{Z}\in\mathcal{C}} \widetilde{\mathcal{L}}_{\log}\left(\Xi^1, ..., \Xi^{p^{\exp}}; \mathbf{Z}\right) \tag{20}$$

where

$$\widetilde{\mathcal{L}}_{\log}\left(\Xi^1, ..., \Xi^{p^{\exp}}; \mathbf{Z}\right) = \sum_{i=1}^{p^{\exp}} \sum_{j=1}^{M} \log_{10}\left[p_{\eta_j}\left(\Xi^i_j, \mathbf{Z}\right)\right] \tag{21}$$

For physical systems, this optimization problem is basically very high-dimensional and it appears that classical deterministic optimization algorithms are not suitable for such an analysis. Moreover, the algebraic constraint defined by Eq. (15) makes genetic algorithms uneffective because this property can not

be reasonably transmitted between two successive generations. Thus, it follows that a random search procedure has to be used in order to solve $\mathcal{R}_3$. The problem is then reduced to **(i)** randomly generate a set of matrices $\mathcal{Z} = \{\mathbf{Z}_i\}_{i=1}^{\mathrm{N^{OPT}}}$ (where $\mathrm{N^{OPT}}$ should be as large as possible) satisfying Eq. (15), **(ii)** evaluate for each $\mathbf{Z}$ the log-likelihood function $\widetilde{\mathcal{L}}_{\log}\left(\Xi^1, ..., \Xi^{p^{\exp}}; \mathbf{Z}\right)$. The general algorithm is as follows [9]:

(i) Procedure for generating the set $\{\mathbf{Z}_i\}_{i=1}^{\mathrm{N^{OPT}}}$:

(1) Randomly generate a matrix $\mathbf{Z}_0$ whose components are independent uniform real random variables in $[-1, 1]$.
(2) Let $\mathbf{Y}_0 = \mathbf{Z}_0\mathbf{Z}_0^{\mathrm{T}}$ and consider its Cholesky decomposition, $\mathbf{Y}_0 = \mathbf{L}^{\mathrm{T}}\mathbf{L}$.
(3) Define $\mathbf{Z}_i$ as: $\mathbf{Z}_i = \mathbf{L}^{-\mathrm{T}}\mathbf{Z}_0$.

(ii) Procedure for estimating the log-likelihood function

(1) Randomly generate realizations of the Gaussian germ $\mathbf{X}$.
(2) Compute the corresponding realizations of η using Eq. (12).
(3) Estimate $\left\{p_{\eta_j}\left(\Xi_j^i, \mathbf{Z}\right)\right\}_{i,j}$ using classical methods.
(4) Compute $\widetilde{\mathcal{L}}_{\log}\left(\Xi^1, ..., \Xi^{p^{\exp}}; \mathbf{Z}\right)$.

Let $\mathbb{M}_{M,Q}(\mathbb{R})$ be the set of all $M \times Q$ real matrices. For $\mathbf{A} \in \mathbb{M}_{M,Q}(\mathbb{R})$, let $\|\mathbf{A}\|_\infty$ be the infinite norm of $\mathbf{A}$ defined by $\|\mathbf{A}\|_\infty = \max_{i=1,...,M} \sum_{j=1}^{Q} |\mathbf{A}_{ij}|$. For $\mathrm{N^{OPT}} = 10000$, the random search procedure is illustrated on Fig. (3), where for each $\mathbf{Z} \in \mathcal{Z}$, the pair $\left(\|\mathbf{Z}\|_\infty, -\widetilde{\mathcal{L}}_{\log}\left(\Xi^1, ..., \Xi^{p^{\exp}}; \mathbf{Z}\right)\right)$ is reported.

3.3 Stochastic solver

The aim of the section is to propose a numerical strategy for solving the stochatic homogenization problem which corresponds to the presented model. More precisely, we want to characterize the macroscopic stochastic stiffness tensor $\widetilde{\widetilde{\mathbb{C}}} = \widetilde{\widetilde{\mathbb{C}}}(\theta)$.

Considering an isotropic composite, one has: $\widetilde{\widetilde{\mathbb{C}}}(\theta) = 3\widetilde{\widetilde{k}}(\theta)\,\mathbb{J} + 2\widetilde{\widetilde{\mu}}(\theta)\,\mathbb{K}$, where $\widetilde{\widetilde{k}}(\theta)$ and $\widetilde{\widetilde{\mu}}(\theta)$ are the stochastic overall bulk and shear moduli of the material respectively ($\mathbb{J} = \frac{1}{3}\boldsymbol{i} \otimes \boldsymbol{i}$, $\mathbb{K} = \mathbb{I} - \mathbb{J}$, $\boldsymbol{i}$ and $\mathbb{I}$ are the second and symmetric fourth-order identity tensors respectively). $\widetilde{\widetilde{k}}(\theta)$ and $\widetilde{\widetilde{\mu}}(\theta)$ are also represented using a Polynomial Gaussian Chaos expansion:

$$\widetilde{\widetilde{k}}(\theta) = \sum_{\chi,|\chi|=1}^{p} k_\chi^c \frac{H_\chi(\mathbf{X})}{\sqrt{\chi!}},\ \widetilde{\widetilde{\mu}}(\theta) = \sum_{\chi,|\chi|=1}^{p} \mu_\chi^c \frac{H_\chi(\mathbf{X})}{\sqrt{\chi!}} \tag{22}$$

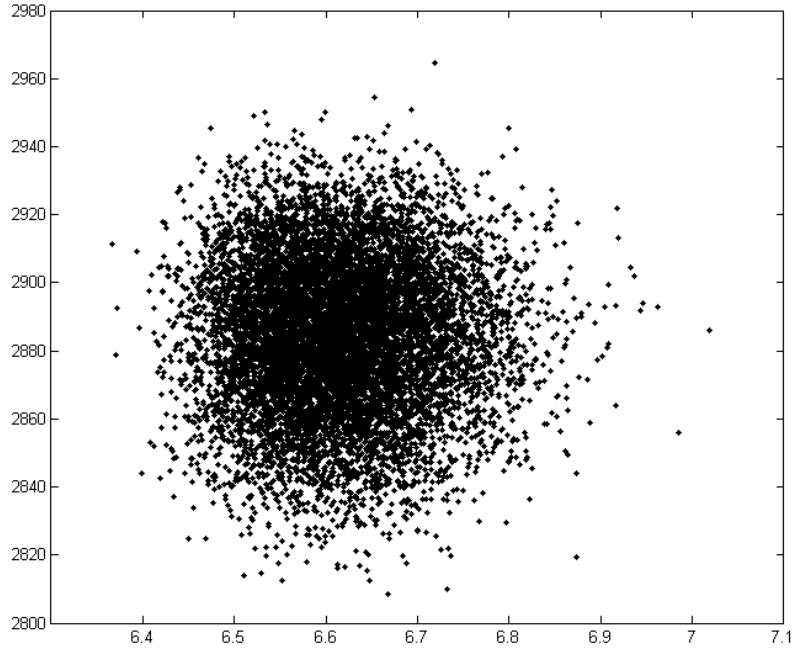

Figure 3. Graph of the pairs $\left(\|\mathbf{Z}\|_{\infty}, -\widetilde{\mathcal{L}}_{\log}\left(\Xi^1, ..., \Xi^{p^{\exp}}; \mathbf{Z}\right)\right)$ for $\mathrm{N}^{\mathrm{OPT}} = 10000$, horizontal axis: $\|\mathbf{Z}\|_{\infty}$, vertical axis: $-\widetilde{\mathcal{L}}_{\log}\left(\Xi^1, ..., \Xi^{p^{\exp}}; \mathbf{Z}\right)$.

The parameters $\left\{k_{\chi}^{c}\right\}_{\chi}$ and $\left\{\mu_{\chi}^{c}\right\}_{\chi}$ are determined using the orthogonality of the Hermite polynomials, that is:

$$k_{\chi}^{c} = \frac{1}{\sqrt{\chi!}} E\left\{\widetilde{\widetilde{k}}\left(\theta\right) H_{\chi}\left(\mathbf{X}\right)\right\},\ \mu_{\chi}^{c} = \frac{1}{\sqrt{\chi!}} E\left\{\widetilde{\widetilde{\mu}}\left(\theta\right) H_{\chi}\left(\mathbf{X}\right)\right\} \tag{23}$$

Note that the computation of the mathematical expectation $E\left\{\widetilde{\widetilde{k}}\left(\theta\right) H_{\chi}\left(\mathbf{X}\right)\right\}$ corresponds to a multi-dimensional integration process:

$$E\left\{\widetilde{\widetilde{k}}\left(\theta\right) H_{\chi}\left(\mathbf{X}\right)\right\} = \int_{\mathbb{R}^m} \widetilde{\widetilde{k}}\left(\theta\right) H_{\chi}\left(\mathbf{x}\right) \phi_m\left(\mathbf{x}\right) d\mathbf{x} \tag{24}$$

where ϕ_m is the m-dimensional canonical normal density. Eq. (24) can be solved by Monte-Carlo numerical simulations [13] which require the computation of the macroscopic moduli for each realization. For each realization of $\mathbf{X}$, Eqs. (6) and (12) provide the realization of the stochastic process $f(\mathbf{x}, \theta_k)$, from which the realization of $F(\mathbf{x}, \theta_k)$ is computed in turn using Eq. (2). Two successive homogenization procedures are then performed and provide the realization $\widetilde{\widetilde{\mathbb{C}}}\left(\theta_k\right)$ (and thus, $\widetilde{\widetilde{k}}\left(\theta_k\right)$ and $\widetilde{\widetilde{\mu}}\left(\theta_k\right)$). Those calculations are performed as follows:

- from the microscale to the meso-scale: for each meso-volume Ω_j $(1 \leq j \leq N^*)$, the volume fraction $F^{(j)}(\theta_k) = F\left(\mathbf{x}, \theta_k, \right),\ \mathbf{x} \in \Omega_j$ is derived from Eqs.

(2) and (6). Then, a mean-field approach or any computational homogenization procedure can be used for estimating the mesoscopic properties (see [15] [26]). Thus, we derive the realizations of the N^* mesoscopic stiffness tensors $\left\{\widetilde{\mathbb{C}}^{(r)}(\theta_k)\right\}_{r=1}^{N^*}$.

- from the meso-scale to the macroscale: once the mesoscopic stiffness tensors have been determined, a suitable linear homogenization scheme can be used in order to determine the overall mechanical properties of the realization of the composite material with random meso-structure.

4 Experimental analysis and micromechanical interpretation

4.1 Principle and application

The experimental identification of the parameters involved in the probabilistic model basically requires the consideration of ν realizations of the microscopic random field. The samples are composite plates defined with respect to a Cartesian coordinate system $(Oxyz)$ (see Fig. (2)). The dimensions in the Ox, Oy and Oz directions are respectively denoted by h_x, h_y et h_z, and are such that $h_z << h_x$ et $h_z << h_y$. The random field is then considered as two-dimensional.
Dealing with a randomly fluctuating volume fraction, a classical method would be to weigh composite samples twice, before and after the resin burn-off. However, such a methodology has two main drawbacks:

(1) it is time-consuming and hardly achievable in practice, taking into account the number of samples that are necessary to achieve converged probabilistic results,
(2) it is a destructive control technique.

Of the above two points, the first one is certainly the most problematic and then, defining another experimental identification procedure turns out to be necessary. The basic idea relies on the fact that in most cases, the matrix and the reinforcing material do have very different ultrasonic properties and thus, one can expect the velocities of some ultrasonic waves (propagating in directions to be determined) to be closely link to the volume fraction. Putting this within a more theoretical framework and recalling that the composite can be considered as isotropic, one introduces the velocity of longitudinal waves propagating inside an isotropic body (see for instance [24]):

$$V_l = \sqrt{\frac{E(1-\nu)}{\rho(1+\nu)(1-2\nu)}} \tag{25}$$

where E, ν and ρ are the Young's modulus, the Poisson ratio and the density of the volume under investigation, respectively.
Since the effective mechanical properties of this volume can be derived from an usual micromechanical analysis (see Fig. (4)), Eq. (25) provides a relation between the volume fraction inside the domain and the velocity of longitudinal waves propagating inside it. It is worth noticing that using such a non-destructive procedure, the size of the meso-volume becomes adaptive.

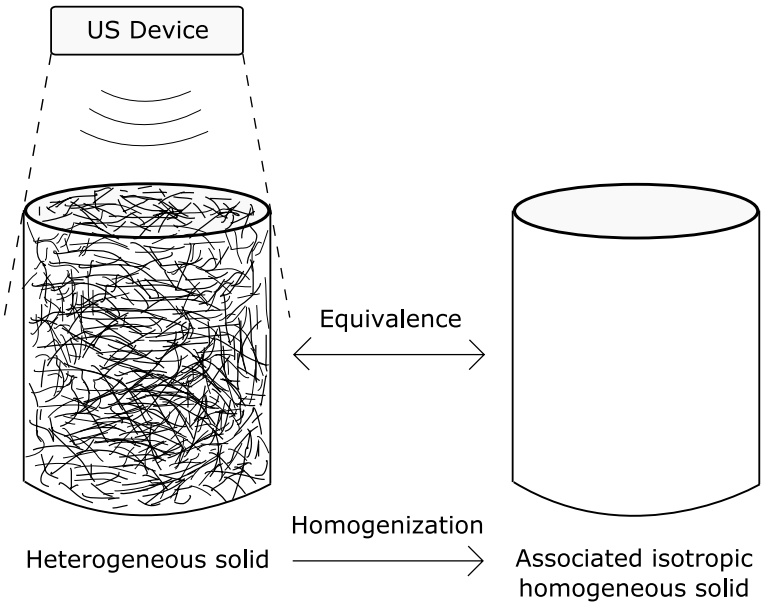

Figure 4. Equivalence between the heterogeneous solid and the associated homogeneous solid.

Remark 1: the methodology can still be applied considering any fiber orientation tensor (and thus, to any anisotropic medium). In this case, the ultrasonic scannings are performed first (a preliminary analysis on the morphology is still necessary to define the waves to be considered) and microstructural information (at least, the distribution and orientation tensors of the fibers) is then determined from classical destructive methods. However, considering anisotropic body significantly complicates the non-destructive analysis, since combinations of different waves have to be considered [24].

Remark 2: note that the injection moulding does not introduce any porosities (which could disturb the ultrasonic testing).

As an application, we consider an isotropic polypropylen matrix reinforced

by long E glass fibers. The properties of each phase are:

$$\begin{cases} E^0 = 1.535\,[GPa],\ \nu^0 = 0.41,\ \rho^0 = 900\,[kg.m^{-3}] \\ E^f = 73\,[GPa],\ \nu^f = 0.21,\ \rho^f = 2600\,[kg.m^{-3}] \end{cases} \tag{26}$$

where the mechanical properties of the matrix were experimentally determined (a database was used for the fibers). Combining Eq. (25) with a micromechanical analysis (detailed in appendix A), one obtains the predictions illustrated on Fig. (5), on which the prediction of a classical rule of mixture on velocities is also reported.

As expected, the function is increasing on the interval of velocities for the

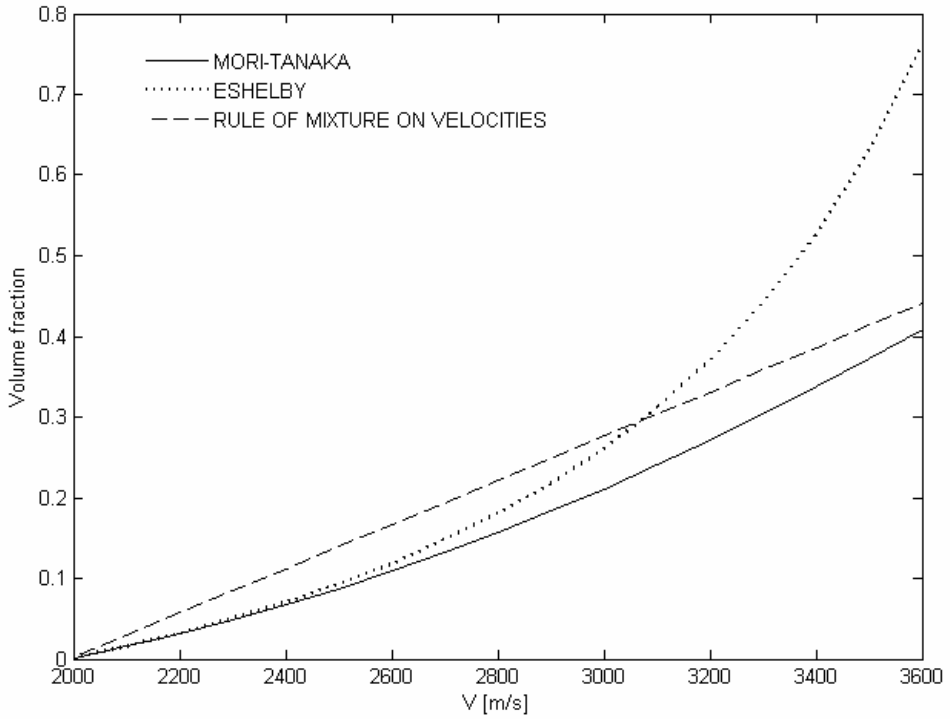

Figure 5. Predictions of the volume fraction using different homogenization schemes.

three estimates which naturally tend to 0 for velocities close to the velocity inside the non-reinforced matrix (around 1991 $m.s^{-1}$). As expected, it is seen that:

- the dilute and Mori-Tanaka estimates coincide for small velocities or equivalently, for small volume fractions (typically less than 0.07),
- the Eshelby's scheme clearly overestimates the volume fraction and is not suitable for the analysis.

It is also interesting to note that for the interval of velocities in consideration (between 1991 $m.s^{-1}$ and 2800 $m.s^{-1}$), the mapping performed using the Mori-Tanaka scheme tends to slightly smooth the resulting random field compared to the one achieved using a simple rule of mixture on velocities (note that this observation is basically reversed for $V > 2900\ m.s^{-1}$ approximately). Thus, the Mori-Tanaka scheme will be used for the mapping between the velocity and volume fraction random fields (see appendix A).
In the following, we consider $p^{\exp} = 110$ realizations of the random field. The ultrasonic sensor used for the analysis investigates a cylindrical volume of diameter $D = 14\ mm$ which is close to the characteric length of the fiber (around $8\ mm$). Samples are composite plates whose total dimensions are $h_x = 260\ mm$, $h_y = 150\ mm$ et $h_z = 3\ mm$ respectively (see Fig. (6) for a general view of the experimental device). The analysis was performed over a reduced domain of length $h_x^{\exp} = 158\ mm$ and width $h_y^{\exp} = 98\ mm$ (see Fig. (7)), finally introducing $N = 84$ micro-volumes.

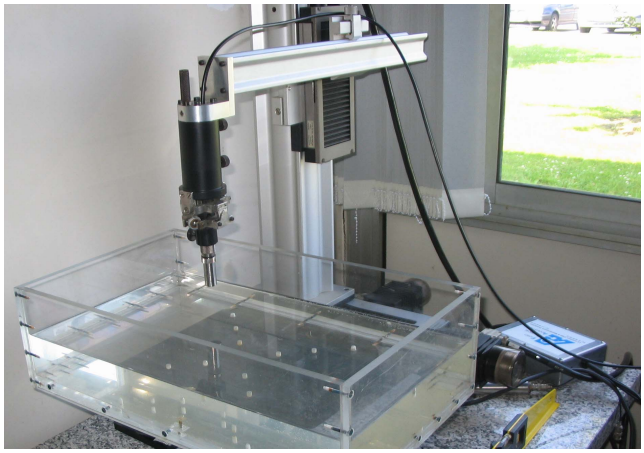

Figure 6. Experimental device: robotic displacement and ultrasonic sensor.

4.2 Experimental results

An experimental realization of the random field f, determined combining the velocity measurements with the micromechanical analysis, is shown on Fig. (8) which illustrates how the volume fraction (at the micro-scale) fluctuates over the composite part. For $\mathbf{x}$ in Ω, the graph of the mean function $\mathbf{x} \mapsto \underline{f}(\mathbf{x})$ is shown on Fig. (9) and demonstrates that the random field realizations do not exhibit any particular boundary effect (see section (4.3)). The correlation

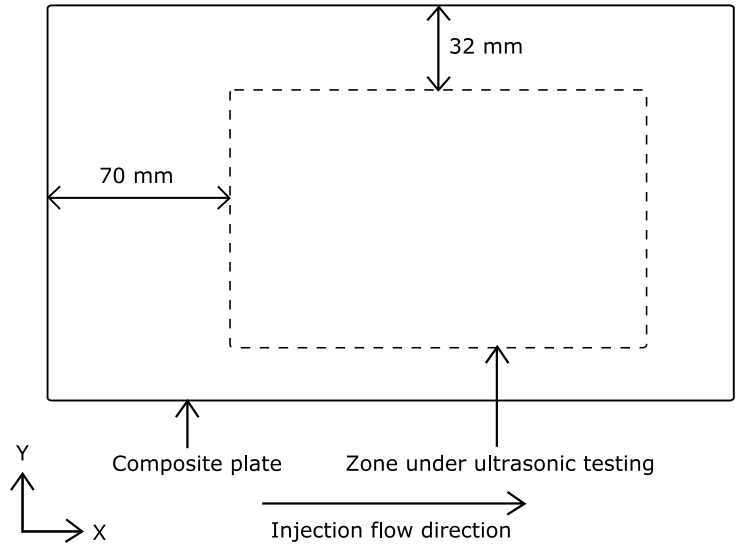

Figure 7. Composite plate and zone under experimental investigation.

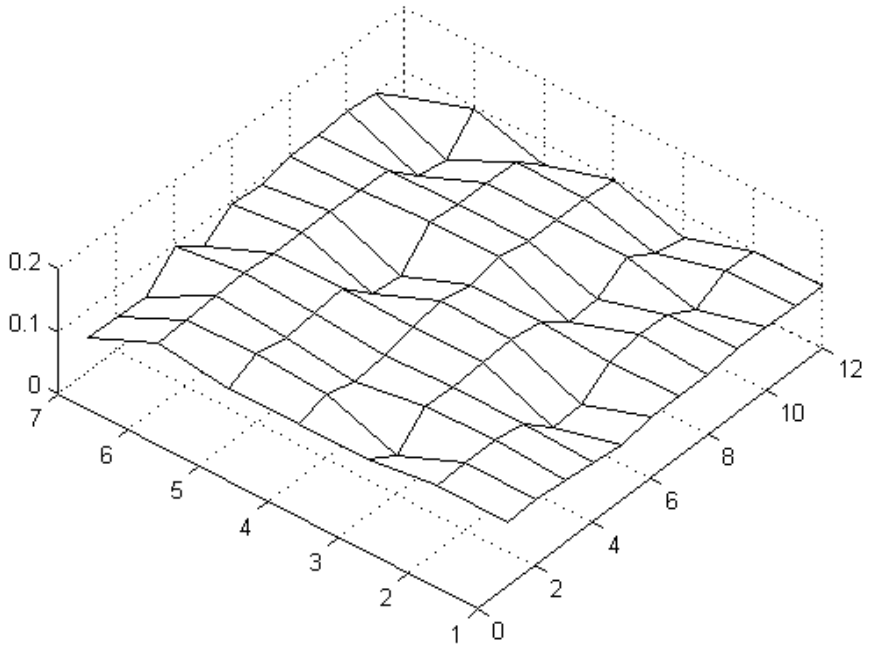

Figure 8. Volume fraction random field, experimental realization 5.

matrix R_f^c, whose components are given by:

$$\left[R_f^c\right]_{ij} = \frac{\widehat{C}_f\left(\mathbf{x}_i, \mathbf{x}_j\right)}{\widehat{\sigma}_f\left(\mathbf{x}_i\right)\widehat{\sigma}_f\left(\mathbf{x}_j\right)} \tag{27}$$

(where $\widehat{\sigma}_f$ is the standard deviation estimate of random field f: $\widehat{\sigma}_f\left(\mathbf{x}_i\right) = \sqrt{\widehat{C}_f\left(\mathbf{x}_i, \mathbf{x}_i\right)}$), is also represented in a meshed view on Fig. (10) (see section (4.3)). Fig. (11) shows the graphs of three marginal probability density esti-

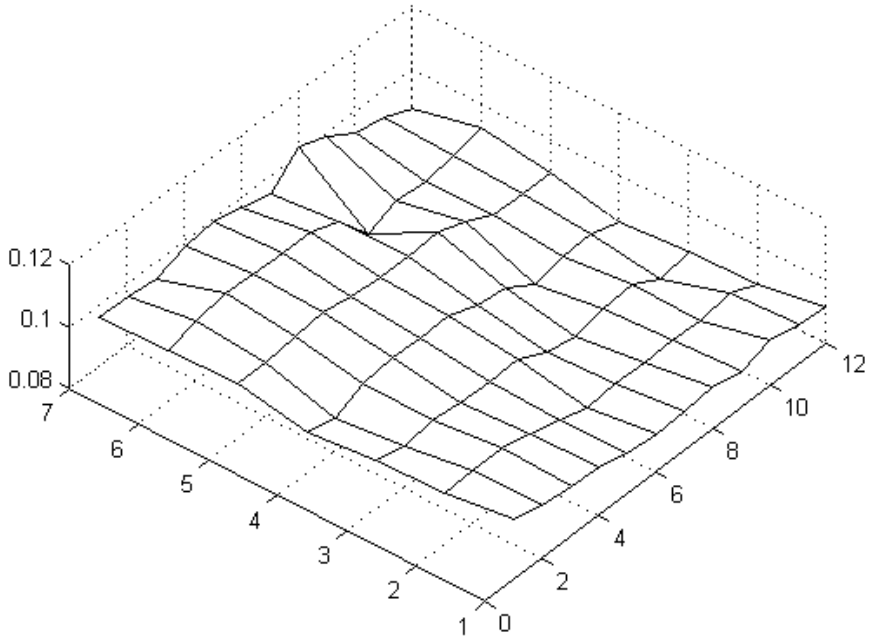

Figure 9. Graph of the mean function $\mathbf{x} \mapsto \underline{f}(\mathbf{x})$.

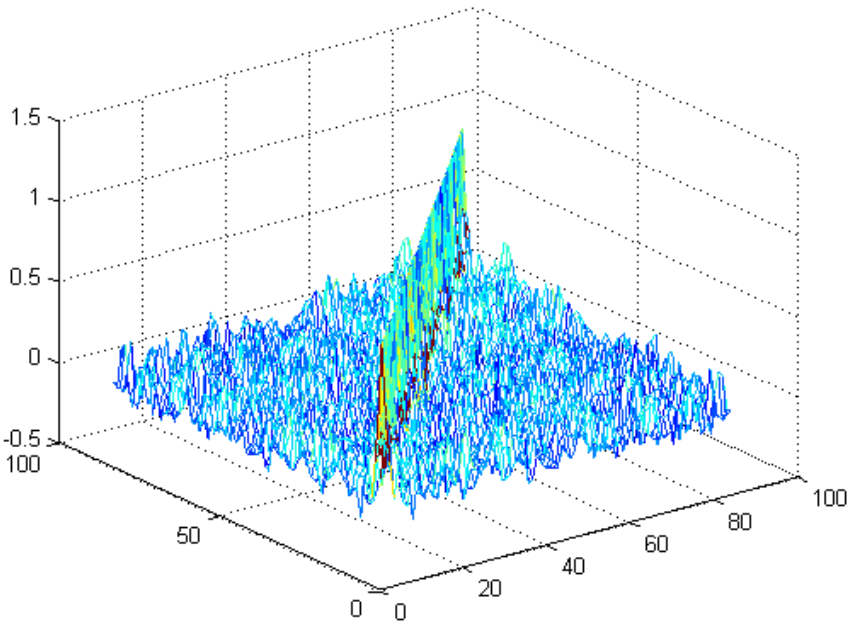

Figure 10. Meshed representation of the correlation matrix.

mates, computed from $\mathcal{S}^{\text{exp}}$ using Eq. (11). The convergence analysis of the statistical reduction is performed using the graph of function $p \longmapsto \sum_{i=1}^{p} \lambda_i^2$ shown on Fig. (12). It is seen that the approximation defined by Eq. (6) can

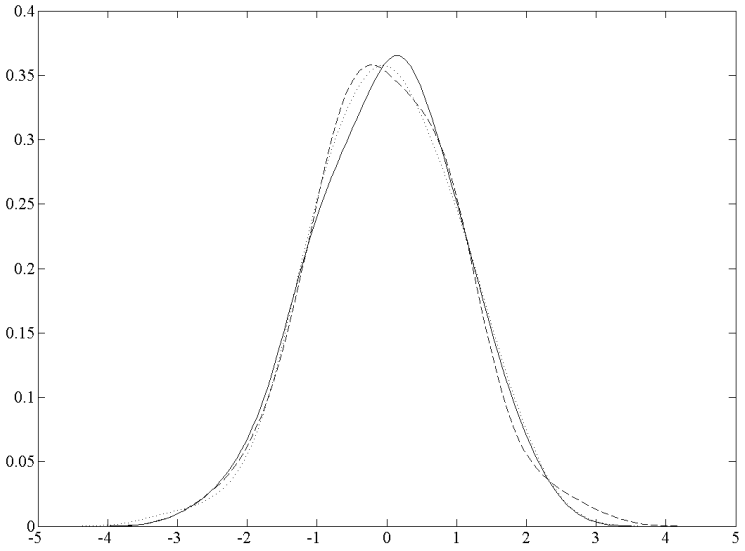

Figure 11. Examples: graphs of the marginal probability density estimates of η_1 (solid line), η_{10} (dashed line) and η_{20} (dotted line).

be reasonably written considering $M = 41$.

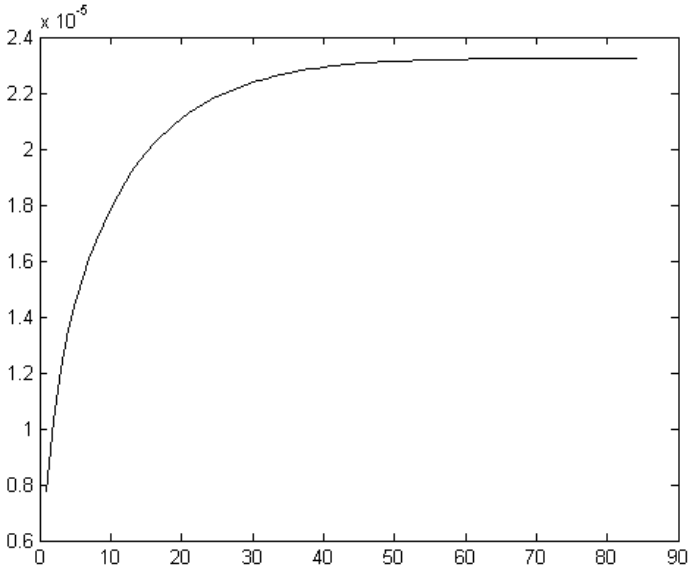

Figure 12. Graph of the function: $p \longmapsto \sum_{i=1}^{p} \lambda_i^2$.

4.3 On the stationarity of the random field

We assume that the domain under investigation is far enough from the edges of the composite plate (see Fig. (7)), so that there is no boundary effect. Then, we assume that the random field f can be approximated by a homogeneous random field f^{s}. Note that this basically results in introducing a model uncertainty that will be discussed in a forthcoming paper. As an illustration, let $\widehat{\underline{f}}$ be the overall mean value estimate, defined by $\widehat{\underline{f}} = \frac{1}{Np^{\exp}} \sum_{i=1}^{N} \sum_{k=1}^{p^{\exp}} f\left(\mathbf{x}_i, \theta_k\right)$. The 2D graph of the mean function is compared to the graph of the overall mean value on Fig. (13). It is readily seen that the mean function slightly fluctuates around $\widehat{\underline{f}}$ (with a coefficient of variation which is less than $5\,\%$) and thus, it can be approximated by the function $\mathbf{x} \mapsto \widehat{\underline{f}}$.

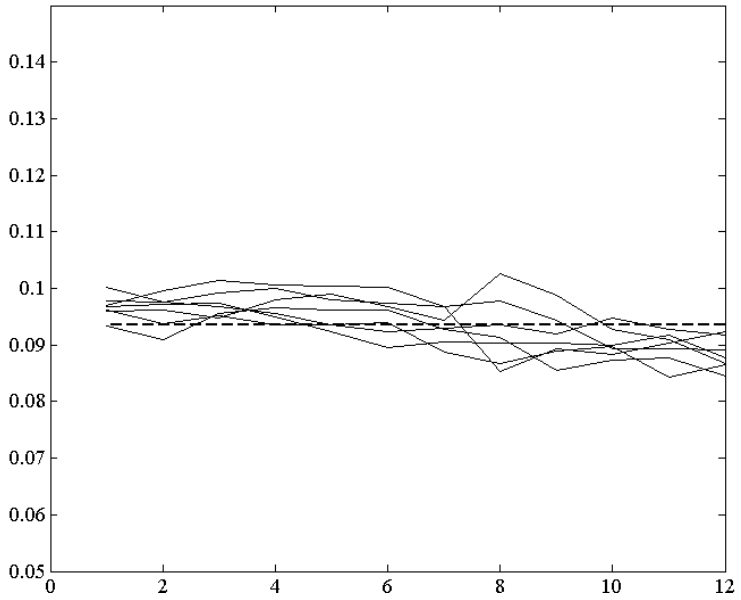

Figure 13. Graphs of the mean functions: $\mathbf{x} \mapsto \underline{f}\left(x, y^i\right)$, $i = 1..7$ (solid lines) and $\mathbf{x} \mapsto \widehat{\underline{f}}$ (dash line).

Then, Eq. (6) becomes:

$$f_{41}^{\mathrm{s}}\left(\mathbf{x}\right) \approx \widehat{\underline{f}} + \sum_{\alpha=1}^{41} \sqrt{\lambda_\alpha} \eta_\alpha \psi_\alpha\left(\mathbf{x}\right) \tag{28}$$

Furthermore, it follows that the correlation function only depends on the relative position of points $\mathbf{x}$ and $\mathbf{x'}$ and is typically formalized using the lag vector $\tau = \mathbf{x} - \mathbf{x'}$ [25]. Considering the experimental data (see Figs. (10), (14)

and (15)), we further assume an exponential correlation structure, so that the normalized correlation function is written as:

$$\rho_f(\tau) = \exp(-\frac{\tau_x}{L_x} - \frac{\tau_y}{L_y}) \tag{29}$$

where τ_u and L_u are the component of τ and the spatial correlation length in the direction u, $u = x$ or y, respectively. Using a classical least-square method, one computes the experimental spatial correlation lengths L_x and L_y:

$$\begin{aligned} L_x^{\exp} &\approx 24\, mm \\ L_y^{\exp} &\approx 6\, mm \end{aligned} \tag{30}$$

The fitted correlation function is illustrated on Fig. (16).

It is interesting to note that $L_x >> L_y$, which is physically consistent (since

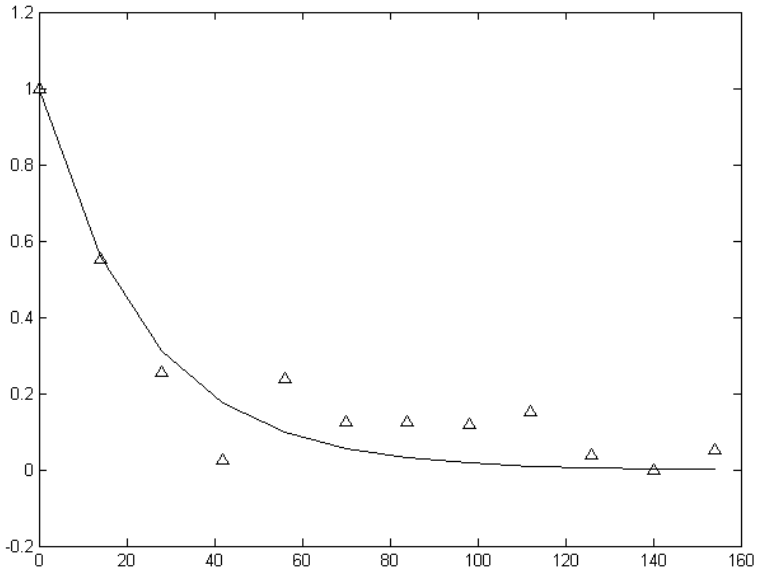

Figure 14. Graph of the function $\tau_x \mapsto \exp(-\tau_x/L_x)$ (marker: experimental value, solid line: modelling), horizontal axis: τ_x.

the flow lines are in the direction x). Furthermore, this result suggests the following conditions on the length a_x and width a_y of the meso-volume:

$$a_x \geq L_x^{\exp},\ a_y \geq L_y^{\exp} \tag{31}$$

and

$$\frac{a_x}{a_y} \approx \frac{L_x^{\exp}}{L_y^{\exp}} \tag{32}$$

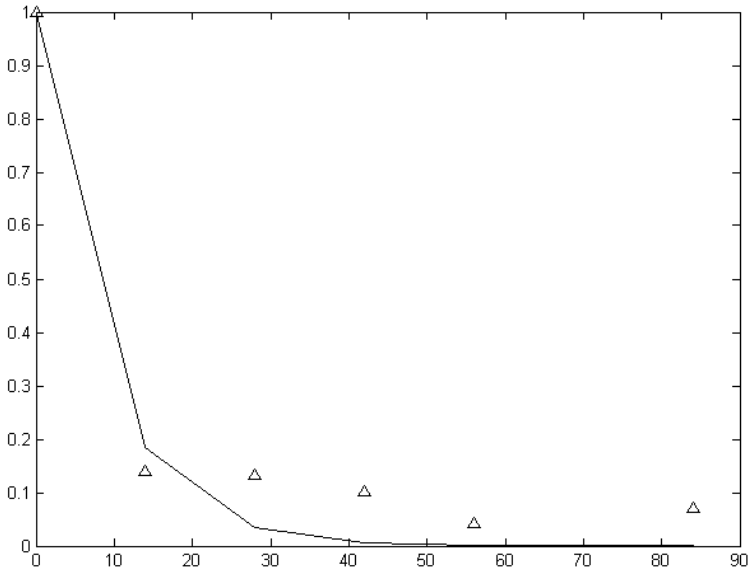

Figure 15. Graph of the function $\tau_y \mapsto \exp(-\tau_y/L_y)$ (marker: experimental value, solid line: modelling), horizontal axis: τ_y.

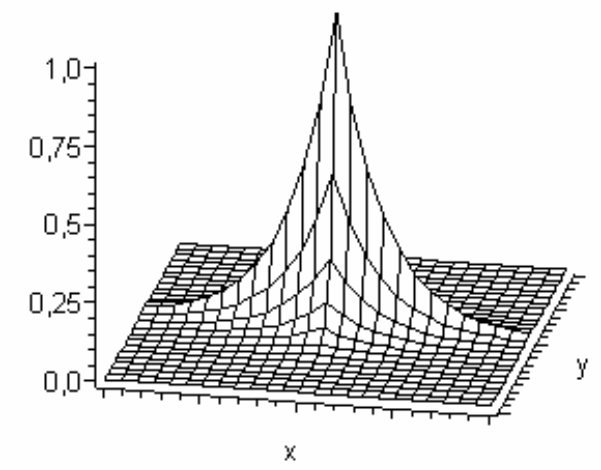

Figure 16. Graph of the correlation function with fitted parameters.

5 Conclusion

The main objective of this study is the characterization of volume fraction stochastic fluctuations in fiber reinforced composites. For this purpose, a theoretical stochastic framework and the associated experimental investigation have been proposed. Relevant scales (namely, the micro-, meso- and macroscale) are first introduced and allows one to proceed to two successive

homogenizations. Then, considering the nature of the fluctuations (along both the spatial axis and the probabilistic dimension), the volume fraction at the microscale is modelled as a random field and the construction of a suitable probabilistic model is proposed.
More precisely, a statistical reduction of the random field is performed using a Karhunen-Loeve expansion and the probabilistic interpolation of the random vector involved in the representation is carried out using a Polynomial Gaussian Chaos expansion. The identification of the Chaos coefficients is classically carried out using the Maximum Likelihood Principle, leading to a high-dimensional optimization problem solved by a random search. Assuming an isotropic elasticity, the random effective bulk and shear moduli are further represented using a Polynomial Gaussian Chaos expansion whose coefficients can be determined coupling the double-scale homogenization procedure with a non-intrusive stochastic solver.
An experimental procedure dedicated to the identification of the parameters involved in the probabilistic model is also presented and relies on velocity measurements (using a non-destructive ultrasonic method). The combination of these experimental results with a micromechanical analysis basically provides realizations of the volume fraction random field. In particular, it is seen that the volume fraction can be modelled by a homogeneous random field whose spatial correlation lengths are determined and may provide conditions on the size of the meso-volumes to be considered. The impact of such volume fraction random fluctuations on the stochastic macroscopic mechanical properties will be presented in a forthcoming paper.

References

[1] Ghanem, R., Spanos, P., "Stochastic finite elements: a Spectral Approach", Springer, New-York, 1991.

[2] Keese, A., "A general purpose framework for stochastic finite elements", PhD Thesis, Technischen Universität Braunschweig, 2004.

[3] Schueller G., "A State-of-the-Art Report on Computational Stochastic Mechanics", Prob. Eng. Mechanics, 12, pp.197-321, 1997.

[4] Ostoja-Starzewski, M., "Material spatial randomness: From statistical to representative volume element", Prob. Eng. Mechanics, 21, pp.112-132, 2006.

[5] Graham, L. L., Baxter, S. C., "Simulation of local material properties based on moving-window GMC", Prob. Eng. Mechanics, 16, pp.295-305, 2001.

[6] Soize, C., "Non Gaussian positive-definite matrix-valued random fields for elliptic stochastic partial differential operators", Computer Methods in Applied Mechanics and Engineering, 195, pp.26-64, 2006.

[7] Coulon, A., "Thermoplastiques renforcés de fibres longues: relations mise en oeuvre/comportement à long terme", PhD Thesis, Université des Sciences et Technologies de Lille, to appear, 2007.

[8] Gărăjeu, M., Suquet, P., "On the influence of local fluctuations in volume fraction of constituents on the effective properties of nonlinear composites. Application to porous materials", Journal of the Mechanics and Physics of Materials, doi: 10.1016/j.jmps.2006.09.005, 2006.

[9] Desceliers, C., Ghanem, R., Soize, C. "Maximum likelihood estimation of stochastic chaos representations from experimental data", Int. J. Numer. Meth. Engng, 66, pp.978-1001, 2006.

[10] Loève, M., "Probability Theory, 4th Ed.", Springer Verlag, New-York, 1977.

[11] Soize, C., Ghanem, R., "Physical systems with random uncertainties: Chaos representations with arbitrary probability measure", SIAM Journal on Scientific Computing, 26 (2), pp.395-410, 2004.

[12] Wiener, N., "The homogeneous chaos", American Journal of Mathematics, 60, pp.897-936, 1938.

[13] Rubinstein, R.Y., "Simulation and the Monte Carlo Method", John Wiley and Sons, New-York, 1981.

[14] Ponte Castañeda, P., Willis, J. R., "The effect of spatial distribution on the effective behavior of composite materials and cracked media", Journal of the Mechanics and Physics of Materials, 43 (12), pp.1919-1951, 1995.

[15] Bornert, M., Bretheau, T., Gilormini, P. (Eds.), "Homogenization in Mechanics of Materials", Iste Publishing Company, 2006.

[16] Field Jr., R. V., Grigoriu, M., "On the accuracy on the polynomial chaos approximation", Prob. Eng. Mechanics, 19, pp.65-80, 2004.

[17] Benveniste, Y. "A new approach to the application of Mori-Tanaka's theory in composite materials", Mechanics of Materials, Vol. 6, pp. 147-157, 1987.

[18] Mori, T. and Tanaka, K. "Average stress in matrix and average elastic energy of materials with misfitting inclusions", Acta Metall., 21, pp. 571-574, 1973.

[19] Mura, T., "Micromechanics of defects in solids", M. Nijhoff Publ., The Hague, The Netherlands, 1987.

[20] Walpole, L. J., "Elastic behavior of composite materials: theoretical foundations", Adv. Appl. Mech., 21, pp. 169-242, 1981.

[21] Ranganathan, S. and Advani, S. G., "Characterization of orientation clustering in short fiber composites", J. of Polymer Science: Part B Polymer Physics, 28, pp. 2651-2672, 1990.

[22] Advani, S. G., "Process Modeling in Composites Manufacturing", Marcel Dekker, New-York, USA, 2002.

[23] Graham-Brady, L. L., Arwade, S. R., Corr, D. J., Gutiérrez, M. A., Breysse, D., Grigoriu, M., Zabaras, N. "Probability and Materials: from Nano- to Macro-Scale: A summary", Prob. Eng. Mechanics, 21, pp.193-199, 2006.

[24] Royer, D. and Dieulesaint, E., "Elastic Waves in Solids, 2nd Ed.", Springer-Verlag, 1999.

[25] Vanmarcke, E. H., "Random Fields : Analysis and Synthesis", MIT Press, Cambridge, 1983.

[26] Nemat-Nasser, S., Hori, S., "Micromechanics: overall properties of heterogeneous materials", North-Holland series in applied mathematics and mechanics, The Netherlands, 1993.

A Micromechanical analysis

The aim of this appendix is to estimate the effective mechanical properties of the volume under consideration and thus, to determine the relation between the volume fraction and the velocity V_l. For this purpose, we consider the Mori-Tanaka estimate (i.e. the matrix is considered as the reference medium and is subjected to its own stress, see [17] [15] [18]), which allows to take into account the interactions between the inhomogeneities. The choice of this homogenization scheme is justified by the "matrix-inclusion" morphology of the studied material as well as by the expected mean volume fraction (lower than 20%). The isotropic effective stiffness tensor $\mathbb{C}^{\text{hom}}$ provided by the Mori-Tanaka scheme is given by:

$$\mathbb{C}^{\text{hom}}_{\text{MT}} = \mathbb{C}^{(0)} + \sum_{r=1}^{N} c^{(r)} \left[\left(\mathbb{C}^{(r)} - \mathbb{C}^{(0)} \right)^{-1} + \mathbb{P}_i^{(r)} \right]^{-1} \left(\sum_{s=0}^{N} c^{(s)} \mathbb{A}_i^{(s)} \right)^{-1} \tag{A.1}$$

where $\mathbb{A}_i^{(s)}$ is the strain concentration tensor for the phase s, defined as:

$$\mathbb{A}_i^{(s)} = \left[\mathbb{I} + \mathbb{P}_i^{(s)} \left(\mathbb{C}^{(s)} - \mathbb{C}^{(0)} \right) \right]^{-1} \tag{A.2}$$

$\mathbb{C}^{(0)}$ is the stiffness tensor of the reference medium (that is, the matrix), $c^{(r)}$ and $\mathbb{C}^{(r)}$ are the volume fraction and the stiffness tensor of phase r, respectively. $\mathbb{P}_i^{(r)}$ is the Hill tensor of the inclusion r (we recall that $\mathbb{P}_i^{(r)} = \mathbb{S}^r_{\text{ESH}} : (\mathbb{C}^0)^{-1}$, where $\mathbb{S}^r_{\text{ESH}}$ is the Eshelby tensor of the inhomogeneity, see [19]) and $\mathbb{I}$ is the symmetric fourth-order identity tensor ($2I_{ijkl} = \delta_{ik}\delta_{jl} + \delta_{il}\delta_{jk}$, where δ_{ij} is the Kronecker delta). Here, a phase r basically corresponds to fibers whose orientation is defined by the same unit normal $\underline{n}^r$. Since fibers differ only in orientation, one has:

$$\forall k \in [1, N]\,,\ \mathbb{C}^{(k)} = \mathbb{C}^{(f)} \tag{A.3}$$

where $\mathbb{C}^{(f)}$ is the stiffness tensor of the fiber. Taking into account interactions between the fibers, one classically introduces the integral form of Eq. (A.1), substituting for instance:

$$\left(\sum_{s=0}^{N} c^{(s)}\mathbb{A}_i^{(s)}\right)^{-1} \longrightarrow \left((1-c)\mathbb{I} + \frac{c}{4\pi}\int_{||\underline{n}||=1} \mathbb{A}_i^{(s)} dS\right)^{-1} \tag{A.4}$$

where c is the volume fraction of fibers inside the volume under consideration. Finally, the effective stiffness tensor is now given by:

$$\begin{aligned}\mathbb{C}_{\mathrm{MT}}^{\mathrm{hom}} = \mathbb{C}^{(0)} + \tfrac{c}{4\pi}\textstyle\int_{||\underline{n}||=1} \left[\left(\mathbb{C}^{(f)} - \mathbb{C}^{(0)}\right)^{-1} + \mathbb{P}_i^{(r)}\right]^{-1} dS \\ \times \left((1-c)\mathbb{I} + \tfrac{c}{4\pi}\textstyle\int_{||\underline{n}||=1} \mathbb{A}_i^{(s)} dS\right)^{-1}\end{aligned} \tag{A.5}$$

We further assume that the curves of the fibers are sufficiently small so that the Eshelby tensor of a straight fiber can be substituted for the one corresponding to a (curved) long fiber (see Fig. (A.1)). Let us now consider the well-known

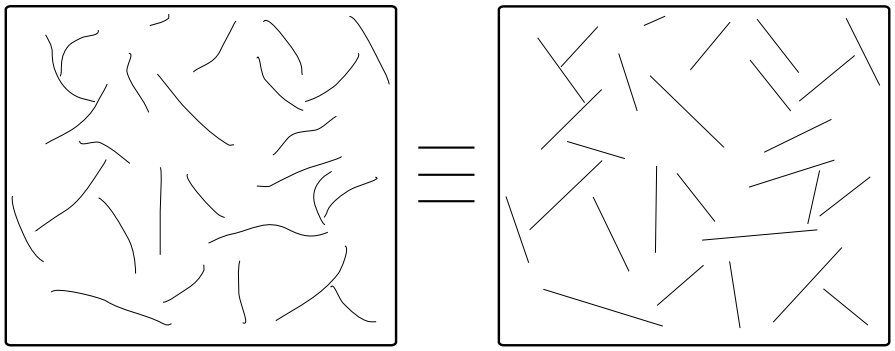

Figure A.1. Schematic of the equivalence between real medium (curved fibers) and modelling (straight fibers).

Walpole basis $\{\mathbb{E}_i\}_{i=1}^{6}$ [20],

$$\begin{aligned}&\mathbb{E}_1 = \tfrac{1}{2}\mathbf{i}_T \otimes \mathbf{i}_T,\ \mathbb{E}_2 = \mathbf{i}_N \otimes \mathbf{i}_N \\ &\mathbb{E}_3 = \mathbf{i}_T \underline{\overline{\otimes}} \mathbf{i}_T - \mathbb{E}_1,\ \mathbb{E}_4 = \mathbf{i}_T \underline{\overline{\otimes}} \mathbf{i}_N + \mathbf{i}_N \underline{\overline{\otimes}} \mathbf{i}_T \\ &\mathbb{E}_5 = \mathbf{i}_N \otimes \mathbf{i}_T,\ \mathbb{E}_6 = \mathbf{i}_T \otimes \mathbf{i}_N\end{aligned} \tag{A.6}$$

where $\mathbf{i}_N = \underline{n} \otimes \underline{n}$, $\mathbf{i}_T = \mathbf{1} - \mathbf{i}_N$ and $2(\mathbf{a}\underline{\overline{\otimes}}\mathbf{b})_{ijkl} = a_{ik}b_{jl} + a_{il}b_{jk}$ for any second-order tensors $\mathbf{a}$ and $\mathbf{b}$. We recall that any transversely isotropic fourth-order

tensor $\mathbb{D}$ can be expressed as:

$$\mathbb{D} = c\mathbb{E}_1 + d\mathbb{E}_2 + e\mathbb{E}_3 + f\mathbb{E}_4 + g\mathbb{E}_5 + h\mathbb{E}_6 = [c, d, e, f, g, h] \tag{A.7}$$

and then, basic tensor operations simply reduce to elementary algebraic operations [20]. Letting by $\{\mathbb{E}_i\}^r$ the basis associated with normal $\underline{n}^r$ and phase r, one has:

$$\mathbb{S}^r_{\text{ESH}} = \left(\frac{1}{2(1-\nu^0)}, 0, \frac{1}{4}\frac{3-4\nu^0}{1-\nu^0}, 0, 0, \frac{\nu^0}{2(1-\nu^0)}\right)_r \tag{A.8}$$

and

$$\left(\mathbb{C}^{(0)}\right)^{-1} = \frac{1}{E^0}\left(1-\nu^0, 1, 1+\nu^0, 1+\nu^0, -\nu^0, -\nu^0\right)_r \tag{A.9}$$

so that:

$$\mathbb{P}^{(r)}_i = \left(\frac{1-\nu^0(1+2\nu^0)}{2E^0(1-\nu^0)}, 0, \frac{(3-4\nu^0)(1+\nu^0)}{4E^0(1-\nu^0)}, 0, 0, 0\right)_r \tag{A.10}$$

where E^0 and ν^0 are the Young's modulus and the Poisson ratio of the isotropic matrix, respectively. Here, the index r means that the Walpole basis is expressed in $\{\mathbb{E}_i\}^r$. It is readily seen that the integration over the unit sphere in Eq. (A.5) basically results in integrating the Walpole basis. Making use of

$$\frac{1}{4\pi}\int_{||\underline{n}||=1} \underline{n}\otimes\underline{n}dS = \frac{1}{3}\mathbf{1},\ \frac{1}{4\pi}\int_{||\underline{n}||=1} \underline{n}\otimes\underline{n}\otimes\underline{n}\otimes\underline{n}dS = \frac{1}{3}\mathbb{J} + \frac{2}{15}\mathbb{K} \tag{A.11}$$

where $\mathbb{J}$ and $\mathbb{K}$ are the classical symmetric fourth-order tensors defined by $\mathbb{J} = \frac{1}{3}\boldsymbol{i}\otimes\boldsymbol{i}$ and $\mathbb{K} = \mathbb{I} - \mathbb{J}$ ($\boldsymbol{i}$ is the second-order symmetric identity tensor : $i_{ij} = \delta_{ij}$), one easily proves that:

$$\begin{aligned} &< \mathbb{E}_1 >= \tfrac{2}{3}\mathbb{J} + \tfrac{1}{15}\mathbb{K},\ < \mathbb{E}_2 >= \tfrac{1}{3}\mathbb{J} + \tfrac{2}{15}\mathbb{K} \\ &< \mathbb{E}_3 >=< \mathbb{E}_4 >= \tfrac{2}{5}\mathbb{K},\ < \mathbb{E}_5 >=< \mathbb{E}_6 >= \tfrac{2}{3}\mathbb{J} - \tfrac{2}{15}\mathbb{K} \end{aligned} \tag{A.12}$$

where $< \mathbb{E}_i >= \frac{1}{4\pi}\int_{||\underline{n}||=1}\mathbb{E}_i dS$. Combining Eqs. (A.1) and (A.12), one derives the effective stiffness tensor $\mathbb{C}^{\text{hom}}$ and then, the overall properties E^{hom} and ν^{hom} (whose expressions are not be provided here, given their complexity). Finally, the density of the composite is obtained from the rule of mixture:

$$\rho^{hom} = c\rho^f + (1-c)\rho^0 \tag{A.13}$$

where ρ^0 and ρ^f are the densities of the matrix and fibers respectively.

Substituting the micromechanical predictions into Eq. (25), one finally defines a function Λ: $c \longrightarrow V_l = \Lambda(c)$ which can be inversed and yields, from a measured velocity field, the corresponding estimate of the volume fraction

field. Note that for each realization of the random field and for each meso-volume Ω_j, one obviously takes $c = F^{(j)}(\theta_k)$ (see section (3.3)).

Remark: assuming that the interactions between fibers are negligible (that is, for $c \longrightarrow 0$), one may consider the dilute scheme, also known as the Eshelby's solution. The corresponding effective stiffness tensor is then given by:

$$\mathbb{C}^{\hom}_{\mathrm{ESH}} = \mathbb{C}^{(0)} + \frac{c}{4\pi} \int_{||\underline{n}||=1} \left[\left(\mathbb{C}^{(f)} - \mathbb{C}^{(0)} \right)^{-1} + \mathbb{P}^{(r)}_i \right]^{-1} dS \tag{A.14}$$

and can be computed using the same methodology as for the Mori-Tanaka estimate.